

Monitoring tidal flat dynamics affected by human activities along an eroded coast in the Yellow River Delta, China

Yaoshen Fan · Shenliang Chen · Bo Zhao ·
Shoubing Yu · Hongyu Ji · Chao Jiang

Received: 21 November 2017 / Accepted: 22 May 2018 / Published online: 12 June 2018
© Springer International Publishing AG, part of Springer Nature 2018

Abstract The coast of the northern Yellow River Delta (YRD) has experienced significant erosion since 1976 due to avulsion and consequent lack of sediment supply. Moreover, massive reclamation activity, expansion of the oil industry, and sea-level rise have jointly contributed to the rapid change of tidal flats over recent decades. Therefore, accurate reporting of the coast spatial extent and stability status is urgently required. We presented a method using remotely sensed waterlines to map tidal flats and monitor their spatiotemporal dynamics. The empirical results show that the area of the intertidal zone west of Tiao River Mouth (TRM)

appeared to be decreasing. Despite intense hydrodynamic force, the intertidal zone to the east of TRM has expanded due to law prohibiting land reclamation in nature reserve. However, this trend weakened due to the expansion of oil industry after 2007. The movement of the mean high-tide line is the main cause for the increase–decrease patterns of the intertidal zone area. To achieve and maintain land equilibrium in this area, we suggest that a 554-m buffer must be preserved for mean high-tide line retreat. Unfortunately, the shrink crisis of the tidal flats has been extremely severe. Future reclamation and oil projects must be supplemented by studies that evaluate the complexities and dynamics of tidal flats so as to prevent the loss of this unique ecosystem.

Highlights

- This is the first study on tidal flats mapping along the eroded coast of the Yellow River Delta ever performed.
- The extent of changes in tidal flats due to human activities were monitored and examined.
- The mean high-tide line movement is the main determinant of tidal flats dynamics.
- Future research will build from this study by addressing the natural complexity of tidal flat systems.

Keywords Tidal flat dynamics · Eroded coast · Human activities · Coastal management · Yellow River Delta

Y. Fan · S. Chen (✉) · H. Ji · C. Jiang
State Key Laboratory of Estuarine and Coastal Research, East
China Normal University, Shanghai 200062, China
e-mail: slchen@sklec.ecnu.edu.cn

B. Zhao
College of Earth, Ocean, and Atmospheric Sciences, Oregon State
University, Corvallis 97331, USA

S. Yu
Yellow River Institute of Hydraulic Research, Yellow River
Conservancy Commission, Zhengzhou 450003, China

Introduction

The morphological evolution of tidal flats has been extensively studied for decades, as healthy mudflats maintain vital ecological and environment functions as well as protect shorelines (Wells et al. 1990; Allard and Michaud 1998; Barbier et al. 2008; Mariotti and Fagherazzi 2010; Ma et al. 2014). Due to the relative sea-level rise (Zhang et al. 2004; Nicholls and Cazenave 2010; Erlandson 2012), decrease of sediment supply from river basins (Syvitski et al. 2009; Wang et al.

2010; Liu et al. 2014; Liu et al. 2017), and changes in nearshore hydrodynamics (Jiménez et al. 1997; Wang et al. 2006; Jia et al. 2014), coasts in different locations worldwide have experienced erosion. This provokes concomitant loss of tidal flats has caused salt marshes to deteriorate (Kirwan and Megonigal 2013). Human activities, such as land reclamation, aquaculture, shoreline protection, and oil exploitation, have promoted a worldwide decline in the extent and health of many intertidal ecosystems (Lotze and Jackson 2006; Airoidi and Beck 2007; Wang et al. 2015; Werf et al. 2015). Therefore, extensive studies on tidal flats are urgently expected since these will provide essential information for understanding coastal response to contemporary environmental shift and human impacts (Yang et al. 2001; Lee et al. 2011).

Regarding coastal monitoring, field surveys are difficult, especially on mudflats, mainly due to their poor accessibility, dearth of shore exposure, and lack of suitable transportation for researchers (Ryu et al. 2008; Xu et al. 2016). The waterline method using satellite images, such as the Landsat Thematic Mapper (TM), Enhanced Thematic Mapper (ETM+), MODIS, and SPOT, provides effective approaches to monitoring shoreline and coastal dynamics (Mason et al. 1995; Kuleli 2010; Ryu et al. 2014; Li and Gong 2016; Sunder et al. 2017). Over the past 30 years, numerous studies have been carried out along the coast of the YRD due to its social and economic value as a unique ecosystem (Cui et al. 2009). Previous studies have primarily focused on the delta shoreline dynamic (Zhang 2011; Kuenzer et al. 2014; Zhang et al. 2016; Fan et al. 2018), erosion–accretion patterns (Cui and Li 2011; Bi et al. 2014; Jiang et al. 2017), and tidal creek changes (Fan and Huang 2004). However, limited attention has been paid to the temporal and spatial extent dynamics of delta tidal flats, especially along an eroding coast under the impact of human activities.

Therefore, we present an approach to waterline calculation using Landsat image. This approach will be applied for monitoring the dynamics of northern YRD, a region within intense hydrodynamic action and human activities. The objectives of this study are (1) developing a methodology to map tidal flats using all available Landsat images, (2) applying this method for analyzing the coast of northern YRD, (3) quantifying spatiotemporal changes of these tidal flats, and (4) discussing how human activities have impacted on tidal flat shrink and future plan on coastal management.

Study area and background

The YRD

The YRD is normally described as the “fan-shaped” area, in which Ninghai serves as its apex. Downstream from Ninghai lies an area of approximately 6000 km² extending from the mouth of the Taoer River in the north to the mouth of the Zhimai River in the south (Fig. 1a). Since 1855, 11 major avulsions have occurred with frequent channel bifurcations. The avulsion occurred in 1976 when the river’s course veered southeastward, resulting in the formation of the active river mouth and the abandoned northern YRD lobe. The Yellow River Delta Nature Reserve (YRDNR) covers an area of approximately 145,000 hm² and forms the second largest coastal wetland in China (Fang and Xu 2000; Kuenzer et al. 2014). The YRDNR consists of two separate parts: the Northern Nature Reserve (NNR) located in the abandoned Yellow River mouth and the Southern Nature Reserve (SNR) in currently active Yellow River mouth (Fig. 1b). The reserve consists of a core zone, a buffer zone, and a test zone (Fig. 1b).

The YRD has been impacted by extensive and rapid human pressures over recent decades (Zhang et al. 2011; Huang et al. 2012). Since the 1980s, humans have been developing crop farming, coastal fisheries, salt industry, and oil exploitation in this area (Yao et al. 2010; Bi et al. 2011). These exploited large portions of natural tidal marshlands due to human constructions and land manipulation (Huang et al. 2012). Over the past 20 years, natural wetland cover has decreased by 38.6% from 2566 km² in 1986 to 1575 km² in 2008 (Wang et al. 2012). The saltmarsh wetland have been reduced by 65.09 km² from 1986 to 2005 (Huang et al. 2012), whereas the constructions on the wetland increased 199.74 km² from 2000 to 2008 (Chen et al. 2011).

The coast of the northern YRD

As part of the abandoned delta lobe, the coast of the northern Yellow River Delta has suffered significant erosion since the avulsion in 1976, and the subsequent discontinuity of sediment supply and the ocean dynamics have become stronger relatively (Li et al. 2000; Chen et al. 2006; Zhang et al. 2016). In addition, the relation between directions of wave and coast has influenced greatly the coastal erosion. From the wave climate offshore the NNR (Fig. 2a), we can conclude that the

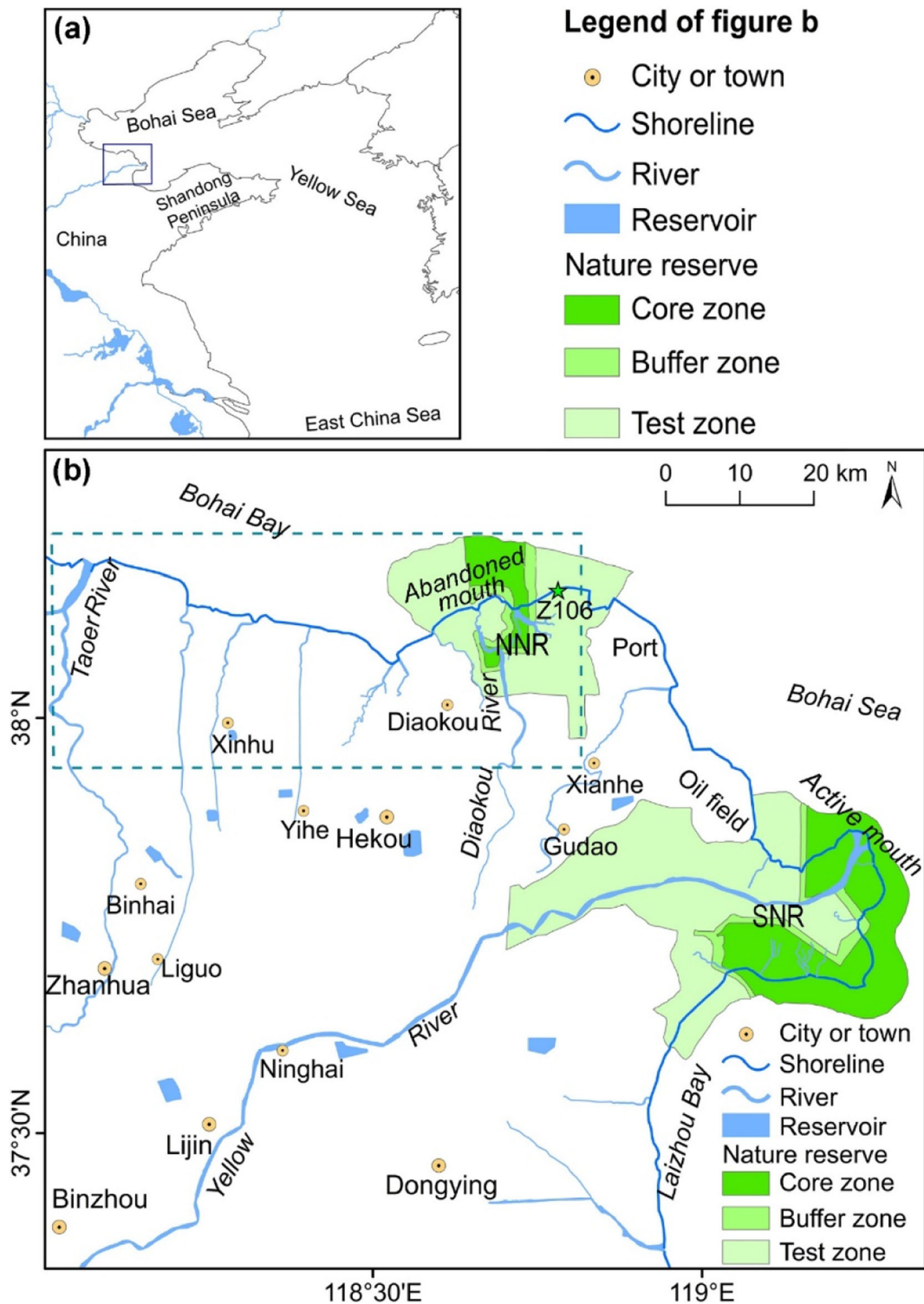


Fig. 1 Range of the Yellow River Delta (YRD), including the Yellow River Delta Nature Reserve (YRDNR)

prevailing direction of waves was NE and the frequency of those wave occurrence was 10.3%. Strong waves

were mainly from NNE to ENE, in which waves from NE were the strongest; waves from NW were secondary.

The whole coast of the northern YRD shows the trend of E–W, which intersected the directions of strong waves and frequent waves, thus strengthening the coastal erosion from wave action. The coast of the YRD locates near the amphidromic point of M2 tidal component (119°03'57"E, 38°08'41"N). The tides of the limited areas around the amphidromic point belong to the regular diurnal tide and then show a transition to the semi-diurnal tide toward south or west. In response to the complex tides, two areas have high current velocity, which are located in the north and the south coast, respectively (Fig. 2b, c). The coast of the northern YRD just happens to be in proximity of the area of high current velocity.

The YRD is continues to bear pressures from oil industry and land reclamation for fisheries and salt industry (Kuenzer et al. 2014; Jin et al. 2016). The 1996 to 2016 reclamation boundaries extracted from Landsat images were compared to a generated fixed line that was roughly parallel to the shoreline (Fig. 3a). The

region area was then calculated to reflect the reclamation development. Figure 3b shows the human reclamation area sustained expansion from 1996 to 2016. Two rapid expansion periods, of 123.98 and 47.26 km²/year, occurred from 2002 to 2003 and from 2011 to 2013, respectively. So far, the reclamation boundary has been advancing into the upper region of the tidal flats (Fig. 3a). To understand the reclamation impacts, the tidal flats in 2000, 2007, and 2015, the years before or after the rapid expansion periods, have been examined in this study.

The coasts to the east of the Z106 drainage station (Z106, see Fig. 4) were protected by concrete levee without tidal flats, so we chose to study the area west of the Z106 and east to the Taoer River Mouth (TERM). Six streamlets and river mouths can be found in the study area, Taoer River Mouth (TERM), Chao River Mouth (CRM), Maxin River Mouth (MRM), Zhanli River Mouth (ZRM), Tiao River Mouth (TRM), and Diaokou River Mouth (DRM). By those river mouths,

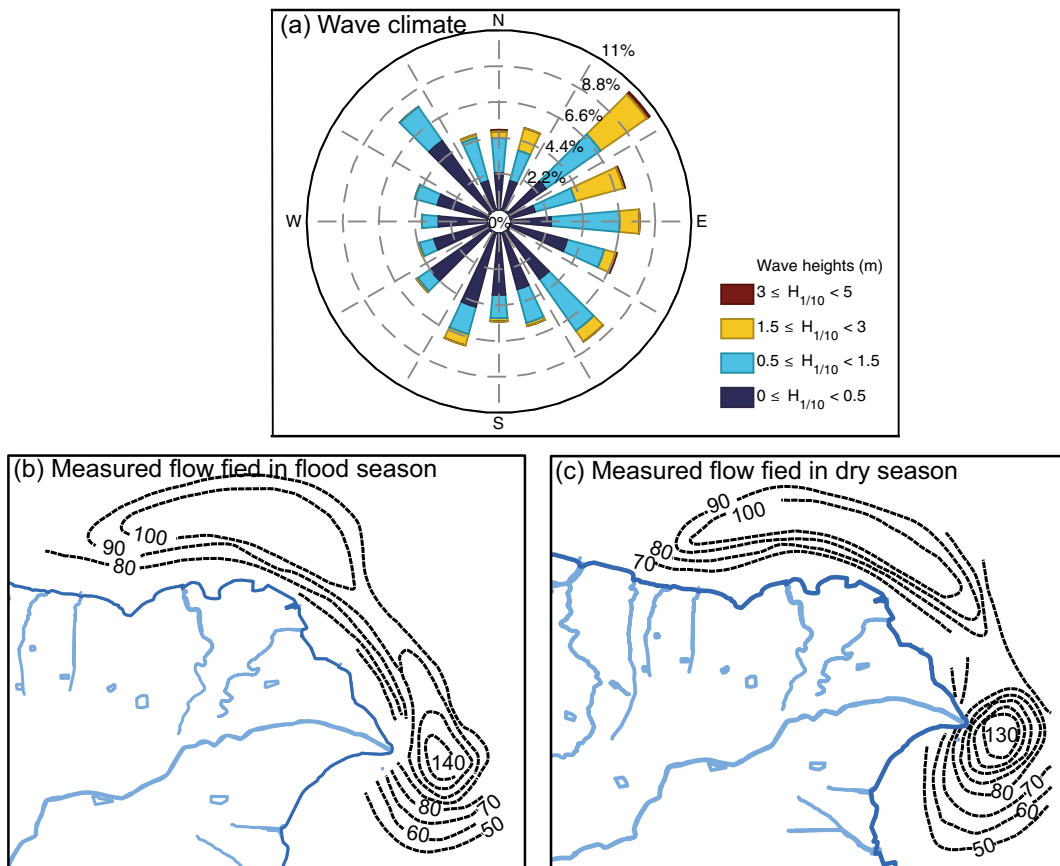


Fig. 2 a The wave climate offshore the NNR. b The hydrodynamic force along the measured flow field (cm/s) along the Yellow River Delta in flood sea, and (c) is in dry season (modified after Hu et al. 1996)

the tidal flats are naturally divided into the six sections, sections A–F (Fig. 4). To understand the spatial dynamics of the tidal flats, we focused on those six sections respectively.

Data and methods

Commonly, tidal flats can be sectioned into three zones by mean high-tide line and mean low-tide line: they are the supratidal zone and the intertidal and the subtidal zones. Since the high- and low-tide lines are time-dependent phenomena that may exhibit short-term variability, this study uses more reliable indicators that specify the “average position” of these two dynamic lines (Boak and Turner 2005) over a period of 3 years. This timeframe is selected to determine if tideline fluctuation could be further linked with human activities and reveal the relative contribution. Thus, we utilize the image data of the representative years (2000, 2007, and 2015), as well as data of their adjacent years (1 year before and 1 year after) are analyzed. For example, the data from 1999 to 2001 were used for 2000 data representative year.

Satellite image and processing

We downloaded all available Landsat TM, ETM, and OLI images (path 121 row 34) of the years under study when cloud cover was approximately 30% from the United States Geological Survey Center for Earth Resources Observation and Science (USGS/EROS). This download obtained a total of 70 (from 1999 to 2001), 83 (from 2006 to 2008), and 98 (from 2014 to 2016) standard Level 1 Terrain-corrected (L1T) images respectively for the tidal flats extracted for 2000, 2007, and 2015. We were able to correct the systematic geometric errors of the L1T images using ground control points and a Digital Elevation Model (DEM) to obtain a geolocation accuracy of better than 0.4 pixels. In order to further reduce the geometric errors resulting from waterline distortion, we used the original geolocation of Landsat 8 OLI image on June 2, 2015 as the benchmark. We then geo-referenced the other images to the fiducial geolocation using the image-to-image module. The Landsat Ecosystem Disturbance Adaptive Processing System (LEDAPS) was utilized as an atmosphere correction tool that converts the at-sensor radiance (digital number, DN) to surface

reflectance to reduce atmospheric effects (Vermote et al. 1997; Masek et al. 2006).

Waterline extraction

We employed several imaging systems to detect the waterline locations. For example, for band selection, the position of the waterline can be affected by a number of driving factors, such as suspended sediment, tidal fluctuations, and the turbidity of water. In this study, we adopted the Normalized Difference Water Index (NDWI) because it provides a greater accuracy (Mcfeeters 1996) and has been demonstrated in highly turbid coastal areas, such as the tidal flats of Bohai Rim (Liu et al. 2016), the tidal flats along the Jiangsu coast in China (Liu et al. 2013), and other intertidal regions across East Asia (Murray et al. 2012). The formulation of NDWI is expressed in the equation below:

$$NDWI = \frac{Green - NIR}{Green + NIR} \quad (1)$$

where “Green” represents the green light band and “NIR” represents the near-infrared band that correspond to the second and fourth bands of Landsat TM/ETM+ image, or the third and fifth bands of the Landsat OLI image. We chose a threshold value based on the algorithm suggested by Otsu (1979) to generate binary image (land–water) from the NDWI image. Application of the dilation and erosion operator of Mathematical Morphology (MM) can close the gap of channels at the boundary of binary image, generating a continuously generated waterline (Geleynse et al. 2012). Figure 6 shows the processes of waterline extraction.

Tidal flat delineation and accuracy assessment

To determine the total extent of the tidal flats, we selected the outermost boundaries of all the waterlines. The mean high- and low-tide lines were distinguished to divide the tidal flats into three zones, namely supratidal zone, intertidal zone, and subtidal zone. An orthogonal transect was generated every approximate 100 m (some places more or less 100 m to ensure orthogonality) along the baseline (Fig. 5a), with each transect and each waterline having an intersection point. These points represented the estimated location (distance from baseline) of the tide at each satellite transit time. Each transect had at

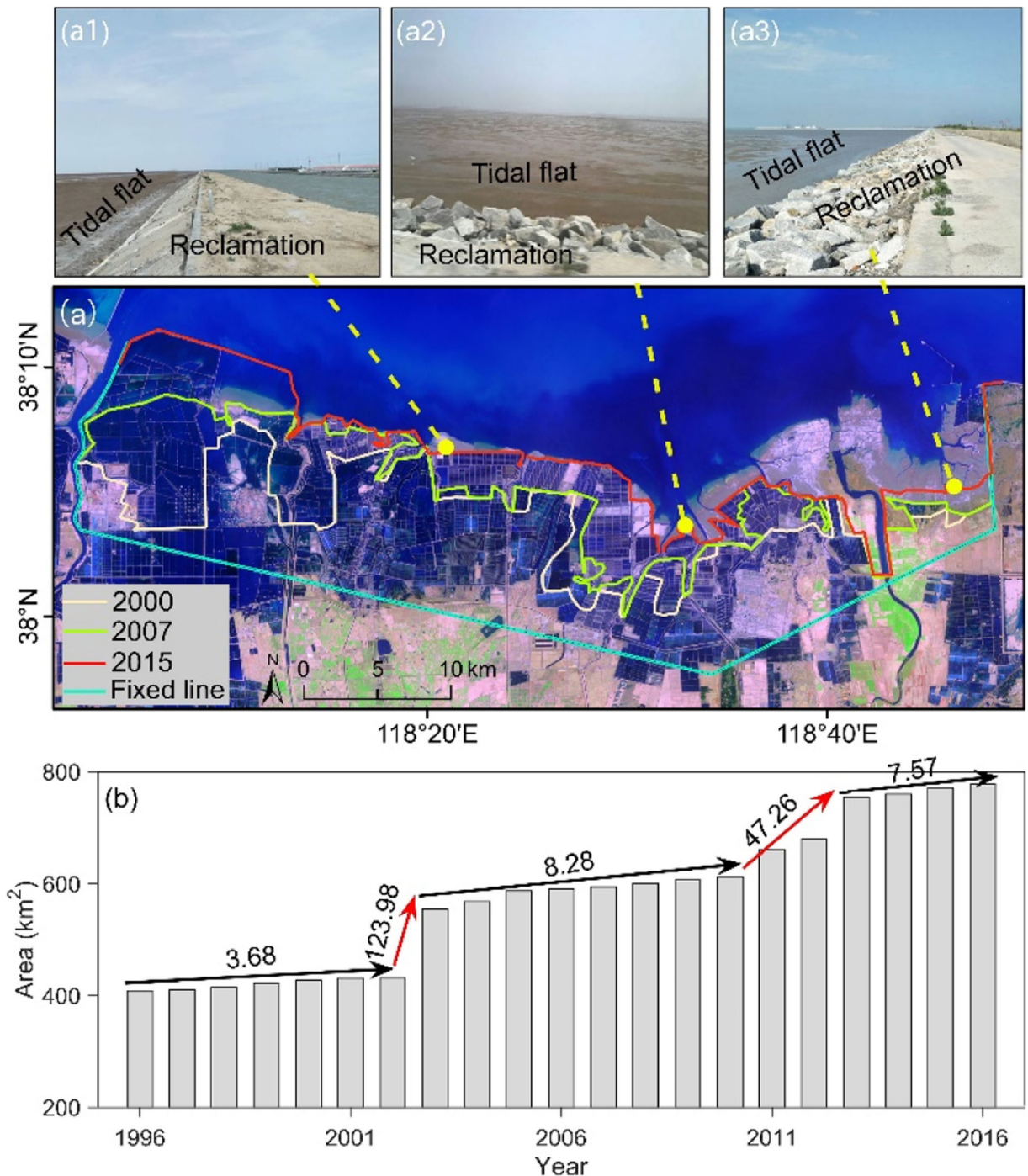


Fig. 3 Reclamation development in the northern YRD. **a** The reclamation boundary of 2000, 2007, and 2015 from Landsat images, including a fixed line that we established to calculate the selected region area. **a1–a3** The reclamation boundary advanced to the upper limit bound of the tidal flats. The photos were taken at

the locations indicated by yellow dots, in August 2017. **b** Changes of selected regions area reflected the reclamation development. The arrows represent an increase in area, and the data on the top represent the rate of increase in square kilometers per year.

least 70 tidal points that we estimated at various times and under various tidal conditions. We calculated the

distance between each tidal point and the baseline. Then, we classified the tidal points based on the

Fig. 4 Map of the coast of the northern Yellow River Delta, including six sections A–F divided by six rivers and river mouths. Bands 7, 5, and 4 from Landsat 8 OLI, acquired in 2015, were combined to form the base map



distances by Jenks Natural Breaks (Jenks 1967) to define high, middle, and low classes. This classification method is a form of data clustering in which the researcher seeks natural “faults” and “discontinuity points” according to intrinsic statistical characteristics of data. This method maximizes variance between classes and minimizes variance within classes to achieve the most accurate classifications.

To determine the most representative segmentations of the mean high-tide and mean low-tide point sets, we first analyzed the data characteristics of tidal points. As shown in Fig. 5b, regardless of the amount of classes, the best segmentation of high- and low-tide point sets was similar. Therefore, distances of tidal points along each transect were divided into three, four, five, and ten classes. Groups containing more than ten classes eliminated the clustering effect of the data. For every transect, the segmentation points of the class that was closest to the baseline and the class that was farthest were selected as segmentation points of the mean high point sets and the mean low point sets, respectively. Thus, we were able to determine the mean high-tide and low-tide lines by linking those points (Fig. 5c).

The accuracy of the extent estimate of tidal flats was assessed by independently comparing reference data with maps in a confusion matrix (Foody 2009). There were 240 sample locations generated utilizing stratified random sampling the non-masked area to establish the two output classes (tidal flat and other). Map data was extracted from the tidal flats map. Reference data was derived by an independent analyst who labeled each sample point as belonging to either a tidal flat or the other class, based on the assessment of available Landsat image of low-tide images and Google Earth image. We then computed the confusion matrix of the resulting map with respect the reference expert data and estimated accuracy measurements that include overall, user’s, and producer’s accuracy.

Analysis of tidal flat dynamics

Three zones within the tidal flats for 2000, 2007, and 2015 were identified and mapped using the method mentioned above. We calculated the net change and growth rate of the intertidal zone areas in different sections. A positive growth rate indicates that the area is increasing, while a negative value means the area is decreasing.

In order to establish detailed change patterns of tidal flats at various spatial scales, we calculated the mean high-tide line change (MHC) and mean low-tide line change (MLC), respectively. We generated a total of 1142 orthogonal profiles spaced at approximate 500 m (some places more or less 500 m to ensure orthogonality) along the baseline. Each transect and each mean high-tide line (or mean low-tide line) had an intersection point, and we determined the MHC (or MLC) based on the distance between the two intersection points.

Results

The mapped tidal flats

Landsat images were utilized to extract the waterline. Figure 6a and b shows the waterline extraction when the turbidity of nearshore were low and high, respectively. The binary images and the waterlines could be generated precisely by NDWI method whatever in low turbidity condition or in high turbidity condition. Based on abovementioned methods, we produced maps for the year 2000, 2007, and 2015. Figure 7 shows the extent of the tidal flats, including reclamation boundaries and river courses. The high-tide images enable us to divide the entire coastline into six sections based on the river mouths. All other regions, such as land, ponds, and deep water are masked off in white.

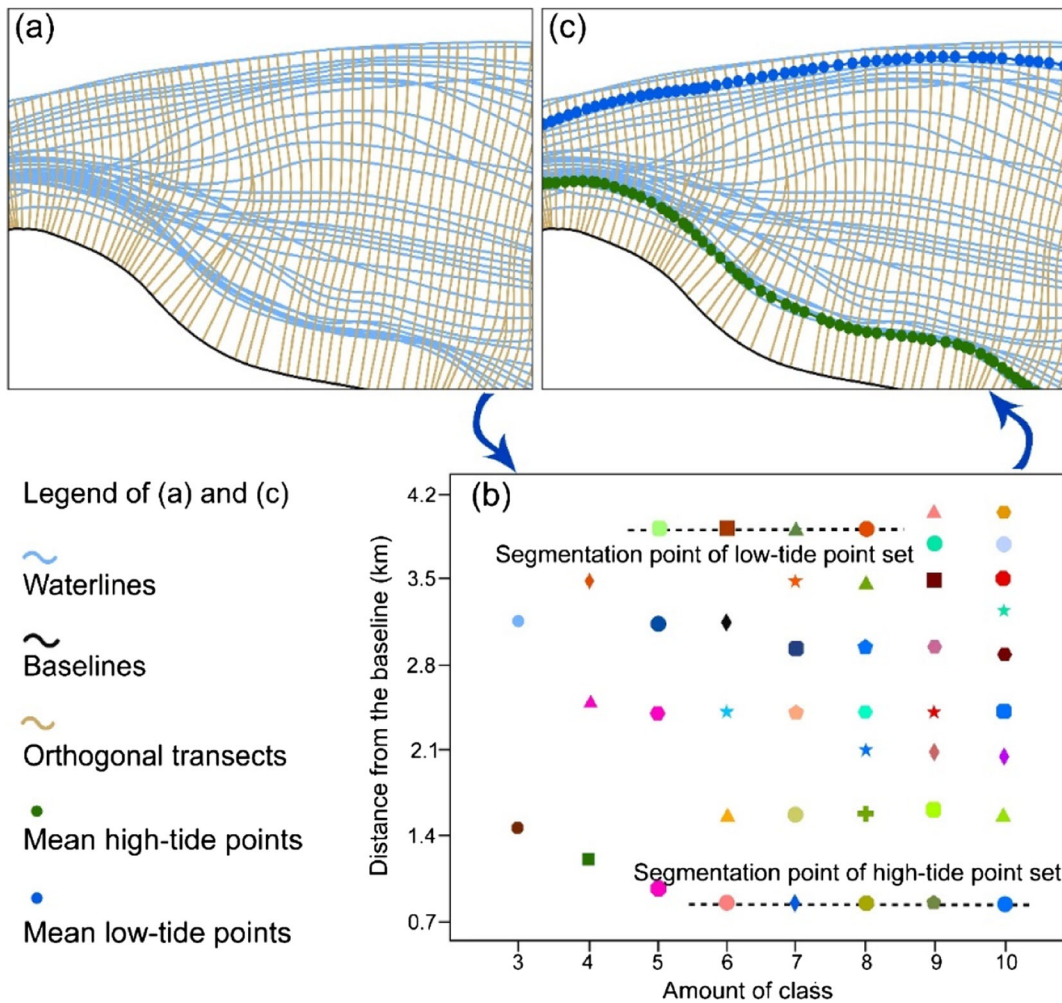


Fig. 5 **a** The waterlines, baseline, and orthogonal transects of the sample area. **b** Relationship between the segmentation point and the amount of class. **c** The mean high-tide points and mean low-tide points were extracted

To assess the accuracy of the estimated extent of tidal flats in 2015, which were calculated from 2014 to 2016 Landsat images, we chose each year’s Landsat 8 OLI low-tide images (Band 8 with a spatial resolution of 15 m), Google Earth images, and field samples (in August, 2017) as references. The confusion matrix is a commonly used tool to assess of accuracy of land cover classification. The matrix scores how the classification process has labeled a series of test sites. The correct land cover of test sites is known. Typically, the true class label is displayed across columns, while the actual mapped class is displayed in columns rows. The diagonal of the confusion matrix displays the number of sample locations for which the true class and the mapped class agree. The overall accuracy of the entire sample is then the sum of the diagonal elements divided

by the total of all sites. For individual classes, the marginal totals of the matrix can estimate the producer’s accuracy and user’s accuracy from the samples. The producer’s accuracy is the probability that a sample truly belonging to class *i* is also mapped as class *i*, while the user’s accuracy is the probability that a sample mapped as class *i* is truly of class *i* (Card 1982).

As shown in Table 1, although the overall classification accuracy for the mapping of tidal flats differed depending on the three reference points, the lowest one was more than 87%, with a user’s accuracy of 89.2% and a producer’s accuracy of 85.6%. Due to the erosion of the coast, the tidal flats near the low-tide line of 2014 may have less coverage. In other words, we may have underestimated the extent of the tidal flats in 2014. The high classification accuracy of the reference image

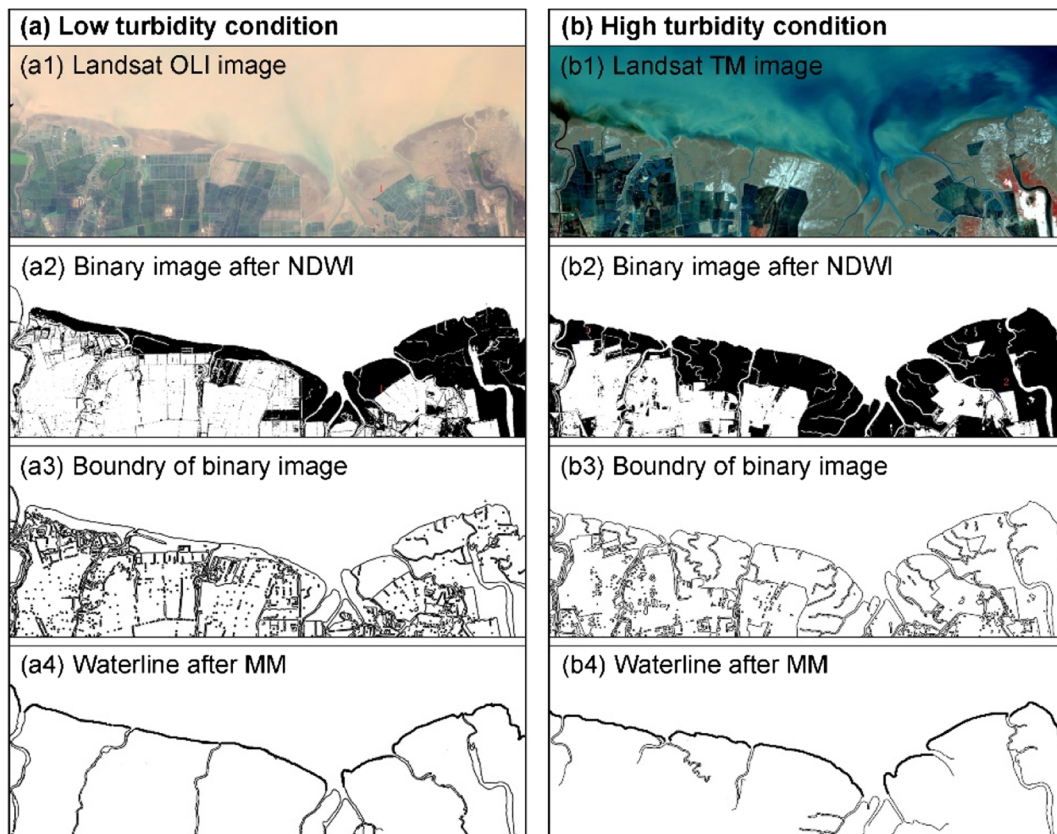


Fig. 6 **a** The processes of waterline extraction under low turbidity condition. **b** The processes of waterline extraction under high turbidity condition. **a1, b1** Landsat image from Landsat 8 OLI, acquired on October 24, 2014 and Landsat image from Landsat 5 TM, acquired on December 11, 2007, respectively. **(a2), (b2), (a3),**

and **(b3)** Landsat images were processed by NDWI and threshold segmentation. **(a4)** and **(b4)** getting the waterline through dilation operator of MM closed the gap of channels and deleting the waterline on the land

in 2016 (Table 1) and the coastal erosion degree indicated that we may have overestimated the extent of the tidal flats in 2016. Thus, the degree of area of the tidal flats, derived from the waterlines of 2014, 2015, and 2016, can be taken as an average of these periods.

The degree of area changes in the intertidal zone

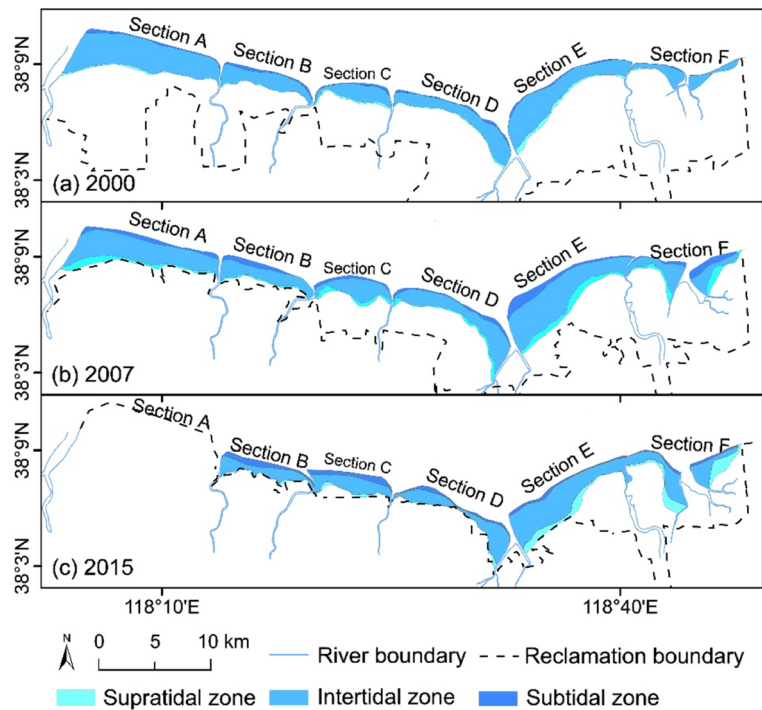
The intertidal zone, as one of the most productive ecosystems on earth, can provide safe spawning areas and nurseries for countless species of fish and crustaceans. This fact led this study to focus primarily on the dynamics of the intertidal zone as a representative of the entire tidal flat region.

The net changes and the growth rates of intertidal zone area were calculated, and the results are shown in Table 2. During the period from 2000 to 2007, the intertidal zone area of sections A, B, and C decreased, while the other

sections increased. Section A showed the most significant decrease with the growth rate of -25.73% . Sections E and F had the largest increase value, with a growth rate of 22.70 and 46.05%, respectively. In the period from 2007 to 2015, the intertidal zone area experienced a significant decrease, except for sections F and C which showed a growth rate of 20.55% and -0.99% (suffered a slight reduction), respectively. The area of section A was reduced to zero, and sections B and C decreased by more than 20%. During the latter period (2007–2015), section F expanded by more than 20%, which was less than in 2000–2007; section E increased after originally decrease with a net increasing of only 1.52 km² and a growth rate of 6.15% by the end of 2015.

The overall growth rate decreased from -2.23% to -33.69% for all sections from the former period (2000–2007) to the latter period (2007–2015). The area of the intertidal zone underwent a significant reduction during

Fig. 7 The spatial extent of tidal flats, with reclamation boundary and river courses of 2002, 2007, and 2015



2007–2015. Throughout the entire research period (2000–2015), only the intertidal zone sections E and F (in the west of the TRM) expanded, whereas the rest of the six

sections diminished. Notably, the land reclamation occupied the intertidal zone of section A, and no new intertidal zone was formed by the end of 2015.

Table 1 Confusion matrix for the mapping of the tidal flat

		Classified		Σ	Producer's accuracy (%)
		Tidal flat	Other		
Reference of 2014	Tidal flat	107	18	125	85.6
	Other	13	102	115	88.7
Σ		120	120	240	
User's accuracy (%)		89.2	85.0		
Overall accuracy (%)					87.2
Reference of 2015	Tidal flat	110	11	121	90.9
	Other	10	109	119	91.6
Σ		120	120	240	
User's accuracy (%)		91.7	90.8		
Overall accuracy (%)					91.3
Reference of 2016	Tidal flat	109	8	117	93.2
	Other	11	112	123	91.1
Σ		120	120	240	
User's accuracy (%)		90.8	93.3		
Overall accuracy (%)					92.2

The matrix shows actual and classified cases in the rows and columns, respectively. The proportion of correctly allocated cases indicates the overall accuracy of the classification system

The spatiotemporal changes of the mean high- and low-tide lines

We further explored the dynamics of mean high- and low-tide lines to further explain this relationship. Figure 8 shows the mean tide lines and their profiles, and Fig. 9 shows the MHC and MLC along each profile. Since a positive MHC or MLC indicates a seaward change and a negative value represents a landward change, we were able to obtain the retreat–advance patterns of the mean high- and low-tide lines from Fig. 9.

During the period from 2000 to 2007, the low-tide line of all six sections moved closer to land due to coastal erosion; however, the direction of high-tide line shift was inconsistent in the six sections. For example, the mean high-tide line in sections A and B shifted closer to sea, while the rest of the six examined sections shifted closer to land. Specifically, the MHC and MLC of sections C and D were almost the same (Table 3). Only the MHC of section E and F were greater than the MLC, which indicated the mean high-tide line experienced more significant retreat than the mean low shift. This phenomenon was consistent with the significant increase of intertidal zone area only in section E and F (Table 2). The average MLC of the six sections was -485.94 m (landward retreat), and the average MHC of all six sections was -321.67 m. This fact indicates that the greater retreat distances of the mean high-tide line in sections E and F could not balance the reverse situation occurring in the other sections.

After 2007, the coast was continually eroded by marine hydrodynamics, and almost all of the mean high- and low-tide lines moved closer to land. Particularly, in sections D and F, both the mean high-tide line and the mean low-tide line showed a significant landward movement. Only in section F, the shift of the mean high-tide line was more than the shift of the mean low-tide line (Table 3), which was consistent with the increase of intertidal zone area only in section F during the period of 2007–2015 (Table 2). The MLC of five sections was -433.14 m, while the MHC of five sections was -264.44 m, which accounted for 61% of the former.

From above, we found that only when the mean high-tide line retreats more distance than the low-tide line, the intertidal zone area could increase. Although intertidal is defined by both mean high- and low-tide lines, the retreat of the mean high-tide line is more likely to be

the principal determinant of the intertidal zone dynamics along this eroded coast. The relationship between the mean high-tide line and intertidal changes, and its impacts on human activities will be discussed in the following section.

Discussion

This study highlights the merits of using remote sensing image to generate precise mapping of tidal flats along the coast of northern Yellow Delta, which has been under intense coastal development. The accuracy assessment indicated a classification rate over 87%. Our approach could (1) be applied for monitoring tidal flats when sufficient Landsat images are available, (2) be incorporated with data obtained from other sensors, permitting a wide range of sensors to meet various objectives, and (3) enable exploration of the human-pressure-driven dynamic patterns, especially along an eroded coast.

Mean high-tide line retreat affected by reclamation

From the empirical results, we observed that both the mean low- and high-tide lines moved landward during our study period. The movements of the mean low-tide line were because of coastal erosion, while the retreats of the mean high-tide line were because of tidal adaptations to morphological changes. The MHC was less than the MLC in sections A and B, during 2002–2007, and sections B–E, during 2007–2015. We observed that the mean high-tide line of these sections collided with the reclamation boundary at the end of these periods, which left no room for retreat (refer to Fig. 7).

Regrading to intertidal zone area in each section during two study periods of 2000–2007 and 2007–2015, significant differences between the MHC and MLC were observed. The connections among the growth rates of the areas of 11 sections (sections A–F during the period of 2000–2007 and sections B–F during the period of 2007–2015) and the difference between the MHC and MLC (refer to Figure 10a). There are obvious positive tendencies between these two variables. The best fit curves are shown in the equations below:

$$y = 0.0565x_1 + 7.7890 \quad R^2 = 0.5971, P < 0.005 \quad (2)$$

where y represents the growth rate of the area and x_1 represents the difference between the MHC and MLC.

Table 2 Area changes and growth rates within intertidal zone of various sections

Period	Area changes	Area of different sections					
		Section A	Section B	Section C	Section D	Section E	Section F
2000–2007	Net change (km ²)	-9.94	-1.23	1.13	0.18	5.61	3.33
	Growth rate (%)	-25.73	-10.65	14.21	1.07	22.70	46.05
2007–2015	Net change (km ²)	-28.69	-2.31	-0.09	-3.84	-4.09	2.17
	Growth rate (%)	-100	-22.38	-0.99	-22.76	-13.49	20.55
2000–2015	Net change (km ²)	-38.63	-3.54	-0.96	-3.66	1.52	5.5
	Growth rate (%)	-100	-30.65	-9.65	-21.93	6.15	76.07

Net change = the last value of a certain period – the initial value of a certain period; growth rate = (net change ÷ the initial value of a certain period) × 100%

This positive correlation is obvious since the retreat-advance combined actions of mean high- and low-tide line define the area of intertidal zones. Figure 10a and Eq. (2) indicate that the growth rate of the area increased with the difference between the MHC and MLC. When the growth rate increases, meaning that the area is enlarging, the landward rate of change for the mean high-tide line is greater than that for the mean low-tide line.

A linear regression analysis between the growth rate of the intertidal zone area and the MHC was performed (Figure 10b). The results suggest a closer relationship between the two variables, except for the MHC in section F. By applying a linear regression (solid line), the relationship between the MHC and

the area growth rate (Fig. 10b) can be indicated by the following equation:

$$y = -0.0364x_2 - 20.1655 \quad R^2 = 0.5220, P < 0.01 \quad (3)$$

where y represents the growth rate of the area and x_2 represents the MHC; R^2 is 0.5220, which is approximately equal to R^2 in Eq. (2). This means that the movement of the mean high-tide line played a critical role in the increase–decrease patterns of the intertidal zone area. According to the linear relationship, we calculated the critical MHC, -554, when the growth rate of the area was 0. This indicates that the 554-m gap should be reserved for the retreat of the mean

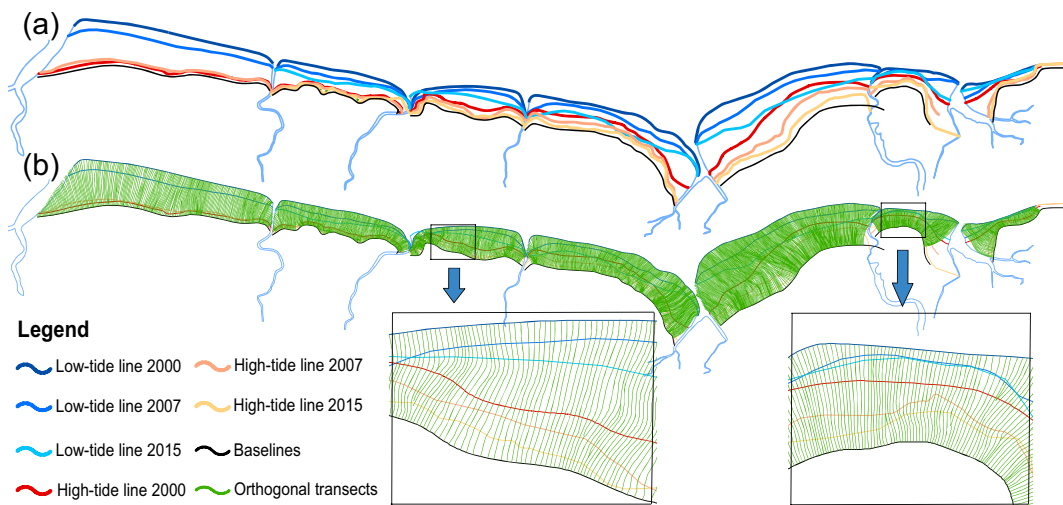
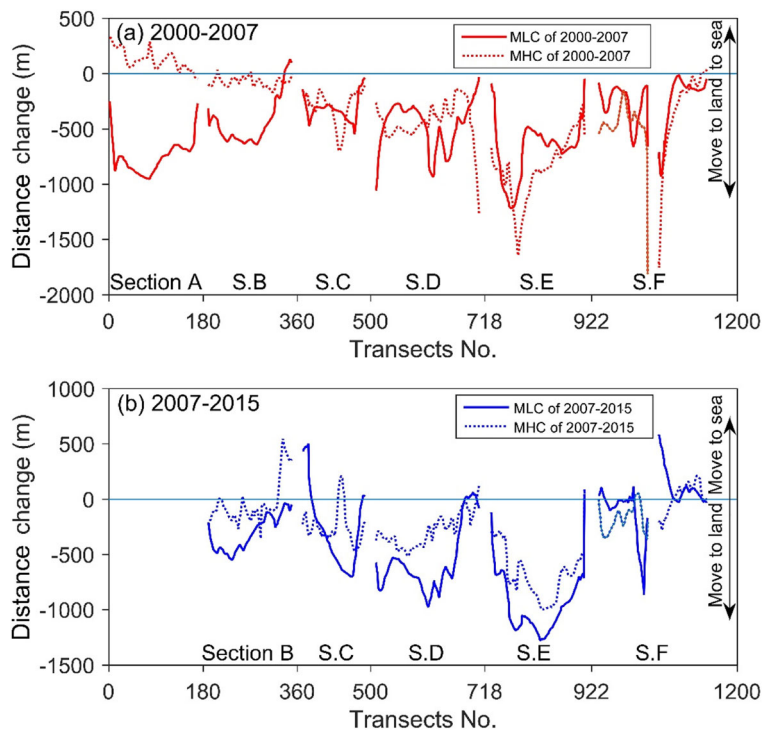


Fig. 8 The mean high- and low-tide lines dynamics from 2000, 2007 to 2015. **a** The location of mean high- and low-tide lines of these three years. **b** A total of 1142 profiles were created along the

coast within a 500-m gap. In addition, two groups of profile samples are shown at a finer scale

Fig. 9 The MHC and MLC in multiple sections during the study periods of 2000–2007 and 2007–2015



high-tide line to maintain equilibrium of the intertidal zone. Unfortunately, the reclamation boundary closed off the mean high-tide line and prevented its retreat in most sections.

Mean high-tide line retreat affected by nature reserve and oil pumps

The NNR, located near the flood plains at the mouth of Diaokou River in the northern delta, occupies 40,000 hm² of the entire reserve. The reserve was approved by the Dongying government in 1990 as an official local nature reserve. It was approved as a national

nature reserve by the State Council of China in October 1992 (Xu 2000). According to the State Council of China, any kind of human activities in the core zone of a national reserve is forbidden. In this nature reserve, we observed that the reclamation boundary did not reach the mean high-tide line and the level of tide line enabled the expansion of the intertidal in sections E and F from 2000 to 2007. Therefore, the setup of the nature reserve contributed to the expansion of the intertidal zone, although the coast has suffered the hydrodynamics-induced erosion.

We observed that the expansion rate in sections E and F decreased after 2007. In addition to the occupation of

Table 3 The MHC and MLC of multiple sections during the study periods of 2000–2007 and 2007–2015

Period	Tidal line	The sectional average MHC and MLC (m)						
		Section A	Section B	Section C	Section D	Section E	Section F	All ^a
2000–2007	Mean low-tide line	-754.45	-438.41	-317.06	-464.53	-686.95	-254.22	-485.94
	Mean high-tide line	122.67	-75.88	-296.88	-431.34	-858.21	-390.38	-321.67
2007–2015	Mean low-tide line	-309	-287.99	-593.95	-963.25	-11.52	-433.14	
	Mean high-tide line	-34.86	-246.97	-286.90	-675.34	-78.12	-264.44	

^aThe last column shows the mean of these sections

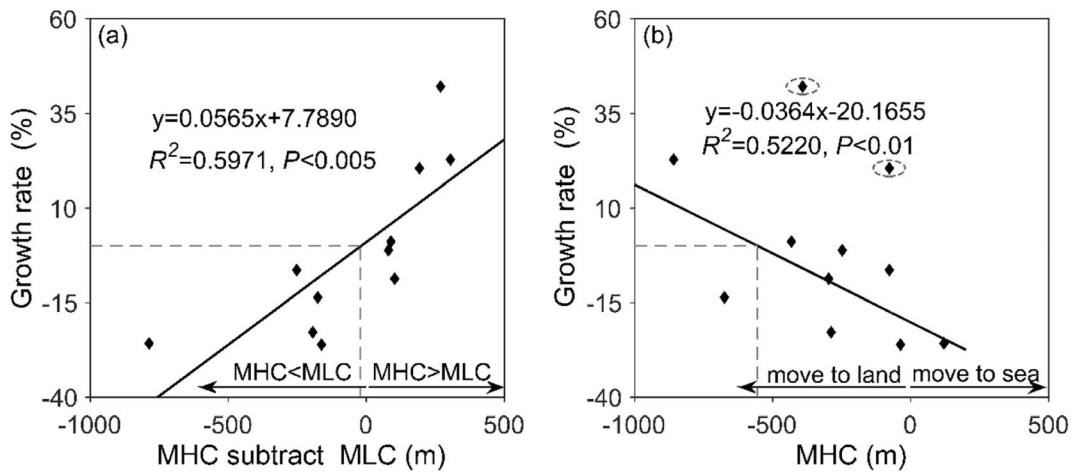


Fig. 10 **a** The area growth rate increased with the difference between the MHC and MLC. **b** Relations between area growth rate and the MHC

the intertidal zone in the west of section E, the oil pumps provoked a negative impact on the expansion of the intertidal zone, especially after 2007. The oil pumps are visible on Google Earth and can also be precisely

located in Landsat image. We analyzed spread of oil pumps within the nature reserve over the course of the study period using the image from Google Earth. Consistent with Kuenzer et al.'s (2014) study, the number of

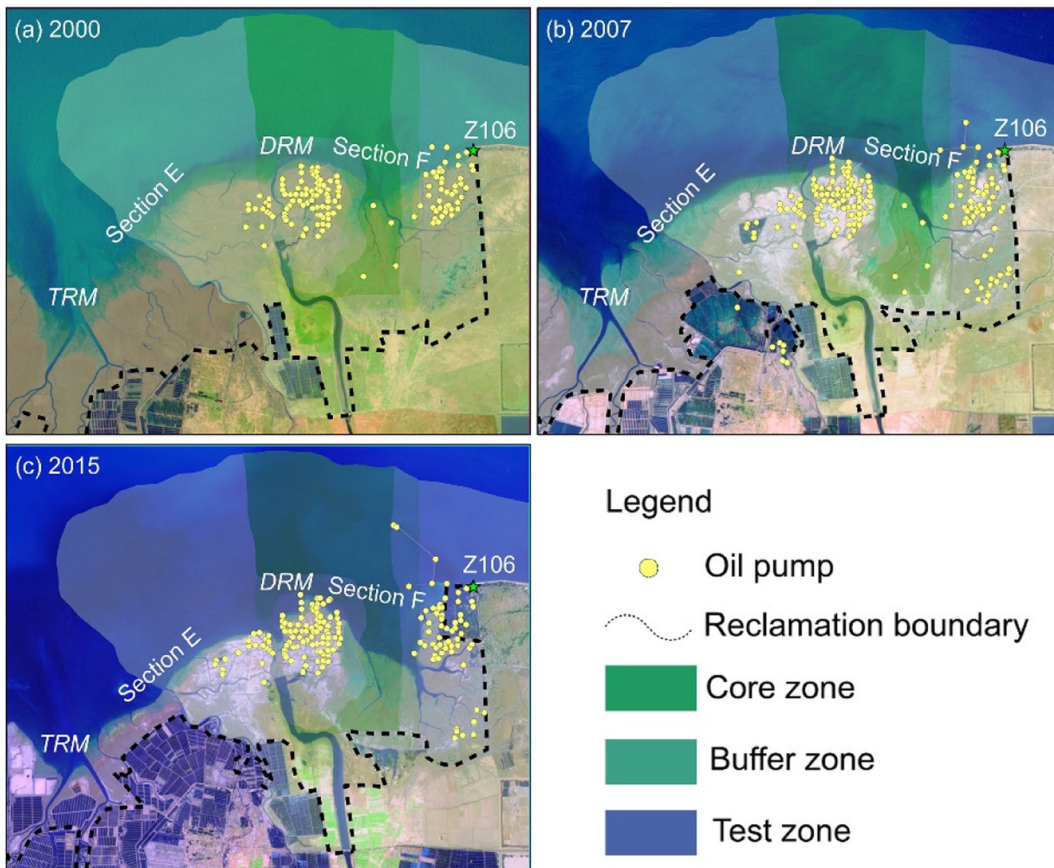


Fig. 11 The locations of oil pumps in the NNR in 2000, 2007, and 2015, including the reclamation boundary

pumps increased from 232 in 2000 to 585 in 2015. In 2000, only a very few oil pumps went over in the wetland area (Fig. 11a). However, the number of pumps increased dramatically in 2007 (Fig. 11b) and 2015 (Fig. 11c) even in the core zone of the nature reserve. The oil pumps connected via road networks prevented the intertidal zone from retreating. From these findings, it is safe to say that it is not enough to terminate reclamation in nature reserves and forbid human activities in the core zones—forbidding oil exploitation in the vicinity of all the tidal flats is also desperately necessary.

Conclusions

In this study, we developed a universal and efficient method for tidal flats mapping using Landsat image. We used a semiautomatic method to extract a series of remotely sensed waterlines. By clustering multiple waterlines within a 3-year period, we were able to identify three distinct zones of the tidal flats for 2000, 2007, and 2015 along an erosive coast under the impact of human activities in YRD.

We divided these tidal flats into six sections (sections A–F) using the five river mouths, and further explored their spatiotemporal dynamics. The empirical results revealed that the area of the intertidal zone to the west of the TRM (sections A–D) appeared to decrease, while the extent of decreased area were inconsistent in these sections. Despite the intense hydrodynamics, the intertidal zone to the east of TRM expanded due to laws prohibiting land reclamation in nature reserves, although this trend has weakened after 2007. The retreat of the mean high-tide line played a critical role in the decreased intertidal zone area. We developed a binary regression model based on the MHC of the 11 sections and the growth rate of the intertidal zone area. This model suggested the mean high-tide line has a 554-m buffer to retreat to maintain area equilibrium of intertidal zones. Although the human land reclamation has come detrimental impacts on mean high-tide line retreat, the expanded of oil industry's profitable activities near the tidal flats also prevented retreat, causing a severe tidal flats crisis. Confronted with abovementioned issues as well as the natural complexity of the YRD tidal flats, interdisciplinary studies that address the multi-annual cycles of the sedimentary processes are necessary to evaluate the impact of human intervention on the coastal environment.

Acknowledgements This study was financially supported by the National Key Research and Development Program of China (No. 2017YFC0405503) and the National Natural Science Foundation of China (No. U1706214). We would like to thank USGS for providing Landsat image. We also appreciate Jin Hu for his assistance in on-site investigation and writing assistance.

References

- Airoldi, L., & Beck, M. W. (2007). Loss, status and trends for coastal marine habitat of Europe. *Oceanography & Marine Biology*, *45*, 345–405.
- Allard, M., & Michaud, Y. (1998). Sedimentology and evolution of subarctic tidal flats along a rapidly emerging coast, eastern Hudson Bay, Canada. *Journal of Coastal Research*, *14*(4), 1242–1254.
- Barbier, E. B., Koch, E. W., Silliman, B. R., Hacker, S. D., Wolanski, E., Primavera, J., Granek, E. F., Polasky, S., Aswani, S., Cramer, L. A., Stoms, D. M., Kennedy, C. J., Bael, D., Kappel, C. V., Perillo, G. M. E., & Reed, D. J. (2008). Coastal ecosystem-based management with nonlinear ecological functions and values. *Science*, *319*(5861), 321–323.
- Bi, X., Wang, B., & Lu, Q. (2011). Fragmentation effects of oil wells and roads on the Yellow River delta, North China. *Ocean & Coastal Management*, *54*(3), 256–264.
- Bi, N. S., Wang, H. J., & Yang, Z. S. (2014). Recent changes in the erosion–accretion patterns of the active Huanghe (Yellow River) delta lobe caused by human activities. *Continental Shelf Research*, *90*, 70–78.
- Boak, E. H., & Turner, I. L. (2005). Shoreline definition and detection: a review. *Journal of Coastal Research*, *21*(4), 688–703.
- Card, D. H. (1982). Using known map category marginal frequencies to improve estimates of thematic map accuracy. *Photogrammetric Engineering & Remote Sensing*, *48*(3), 431–439.
- Chen, S. L., Zhang, G. A., & Chen, X. Y. (2006). Coastal erosion feature and mechanism at Feiyantan in the Yellow River delta. *Marine Science Bulletin*, *8*(1), 11–20.
- Chen, J., Wang, S. Y., & Mao, Z. P. (2011). Monitoring wetland changes in Yellow River delta by remote sensing during 1976–2008. *Progress in Geography*, *30*(5), 585–592 (in Chinese).
- Cui, B. L., & Li, X. Y. (2011). Coastline change of the Yellow River estuary and its response to the 638 sediment and runoff (1976–2005). *Geomorphology*, *127*(1–2), 32–40.
- Cui, B., Yang, Q., Yang, Z., & Zhang, K. (2009). Evaluating the ecological performance of wetland restoration in the Yellow River Delta, China. *Ecological Engineering*, *35*(7), 1090–1103.
- Erlanson, M. V. (2012). As the world warms: Rising seas, coastal archaeology, and the erosion of maritime history. *Journal of Coastal Conservation*, *16*(2), 137–142.
- Fan, H., & Huang, H. (2004). Spatial-temporal changes of tidal flats in the Huanghe River delta using Landsat TM/ETM+ images. *Journal of Geographical Sciences*, *14*(3), 366–374.

- Fan, Y. S., Chen, S. L., Zhao, B., Pan, S. Q., Jiang, C., & Ji, H. Y. (2018). Shoreline dynamics of the active Yellow River delta since the implementation of water-sediment regulation scheme: A remote-sensing and statistics-based approach. *Estuarine Coastal and Shelf Science*, 200, 406–419.
- Fang, H., & Xu, J. (2000). Land cover and vegetation change in the Yellow River Delta nature reserve analyzed with Landsat Thematic Mapper data. *Geocarto International*, 15(4), 43–50.
- Foody, G. M. (2009). Sample size determination for imagery classification accuracy assessment and comparison. *International Journal of Remote Sensing*, 30(20), 5273–5291.
- Geleynse, N., Voller, V. R., Paola, C., & Ganti, V. (2012). Characterization of river delta shorelines. *Geophysical Research Letters*, 39(17), L17402.
- Hu, C. H., Ji, Z. W., & Wang, T. (1996). Characteristics of ocean dynamics and sediment diffusion in the Yellow River estuary. *Journal of Sediment Research*, 4, 1–10 (In Chinese).
- Huang, L., Bai, J., Chen, B., Zhang, K., Huang, C., & Liu, P. (2012). Two-decade wetland cultivation and its effects on soil properties in salt marshes in the Yellow River delta. *China Ecological Informatics*, 10(7), 49–55.
- Jenks, G. F., 1967. The data model concept in statistical mapping. *International Yearbook of Cartography*.
- Jia, Y. G., Zheng, J. W., Yue, Z. Q., Liu, X. L., & Shan, H. X. (2014). Tidal flat erosion of the Huanghe River Delta due to local changes in hydrodynamic conditions. *Acta Oceanologica Sinica*, 168(7), 116–124.
- Jiang, C., Pan, S. Q., & Chen, S. L. (2017). Recent morphological changes of the Yellow River (Huanghe) submerged delta: Causes and environmental implications. *Geomorphology*, 293, 93–107.
- Jiménez, J., Sánchez-Arcilla, A., Valdemoro, H. I., Gracia, V., & Nieto, F. (1997). Processes reshaping the Ebro delta. *Marine Geology*, 144(1–3), 59–79.
- Jin, Y., Yang, W., Sun, T., Yang, Z., & Li, M. (2016). Effects of seashore reclamation activities on the health of wetland ecosystems: A case study in the Yellow River delta, China. *Ocean & Coastal Management*, 123, 44–52.
- Kirwan, M. L., & Megonigal, J. P. (2013). Tidal wetland stability in the face of human impacts and sea-level rise. *Nature*, 504(7478), 53–60.
- Kuenzer, C., Ottinger, M., Liu, G. H., Sun, B., Baumhauer, R., & Dech, S. (2014). Earth observation-691 based coastal zone monitoring of the Yellow River delta: Dynamics in China's second largest 692 oil producing region observed over four decades. *Applied Geography*, 55, 92–107.
- Kuleli, T. (2010). Quantitative analysis of shoreline changes at the Mediterranean coast in Turkey. *Environmental Monitoring & Assessment*, 167(1–4), 387–397.
- Lee, Y. K., Ryu, J. H., Choi, J. K., Soh, J. G., Eom, J. A., & Won, J. S. (2011). A study of decadal sedimentation trend changes by waterline comparisons within the Ganghwa tidal flats initiated by human activities. *Journal of Coastal Research*, 27(5), 857–869.
- Li, W. Y., & Gong, P. (2016). Continuous monitoring of coastline dynamics in western Florida with a 30-year time series of Landsat imagery. *Remote Sensing of Environment*, 179, 196–209.
- Li, G., Zhuang, K., & Wei, H. (2000). Sedimentation in the Yellow River delta. Part III: Seabed erosion and diapirism in the abandoned subaqueous delta lobe. *Marine Geology*, 168(1), 129–144.
- Liu, Y., Li, M., Mao, L., Cheng, L., & Chen, K. (2013). Seasonal pattern of tidal-flat topography along the Jiangsu Middle Coast, China, using HJ-1 optical images. *Wetlands*, 33(5), 871–886.
- Liu, F., Yuan, L. R., Yang, Q. S., Ou, S. Y., Xie, L. L., & Cui, X. (2014). Hydrological responses to the combined influence of diverse human activities in the Pearl River delta. *China Catena*, 113, 41–55.
- Liu, X., Gao, Z., Ning, J., Yu, X., & Zhang, Y. (2016). An improved method for mapping tidal flats based on remote sensing waterlines: a case study in the Bohai Rim, China. *IEEE Journal of Selected Topics in Applied Earth Observations & Remote Sensing*, 9(11), 5123–5129.
- Liu, F., Chen, H., Cai, H. Y., Luo, X. X., Ou, S. Y., & Yang, Q. S. (2017). Impacts of ENSO on multiscale variations in sediment discharge from the Pearl River to the South China Sea. *Geomorphology*, 292, 24–36.
- Lotze, H. K., & Jackson, J. B. C. (2006). Depletion, degradation, and recovery potential of estuaries and coastal seas. *Science*, 312(5781), 1806–1809.
- Ma, Z., Melville, D. S., Liu, J., Chen, Y., Yang, H., Ren, W., Zhang, Z., Piersma, T., & Li, B. (2014). Rethinking China's new great wall. *Science*, 346(6212), 912–914.
- Mariotti, G., & Fagherazzi, S. (2010). A numerical model for the coupled long-term evolution of salt marshes and tidal flats. *Journal of Geophysical Research: Atmospheres*, 115(115), 195–205.
- Masek, J. G., Vermote, E. F., Saleous, N. E., Wolfe, R., Hall, F. G., Huemmrich, K. F., Gao, F., Kutler, J., & Lim, T. (2006). A Landsat surface reflectance dataset for North America, 1990–2000. *IEEE Geoscience & Remote Sensing Letters*, 3(1), 68–72.
- Mason, D., Davenport, I., Robinson, G., Flather, R., & McCartney, B. (1995). Construction of an inter-tidal digital elevation model by the 'water-line' method. *Geophysical Research Letters*, 22(23), 3187–3190.
- Mcfeeters, S. K. (1996). The use of the Normalized Difference Water Index (NDWI) in the delineation of open water features. *International Journal of Remote Sensing*, 17(7), 1425–1432.
- Murray, N. J., Phinn, S. R., Clemens, R. S., Roelfsema, C. M., & Fuller, R. A. (2012). Continental scale mapping of tidal flats across East Asia using the Landsat archive. *Remote Sensing*, 4(11), 3417–3426.
- Nicholls, R. J., & Cazenave, A. (2010). Sea-level rise and its impact on coastal zones. *Science*, 328, 1517–1520.
- Otsu, N. (1979). A threshold selection method from gray-level histograms. *IEEE Transactions on Systems, Man and Cybernetics*, 9, 62–66.
- Ryu, J. H., Kim, C. H., Lee, Y. K., Won, J. S., Chun, S. S., & Lee, S. (2008). Detecting the intertidal morphologic change using satellite data. *Estuarine Coastal & Shelf Science*, 78(4), 623–632.
- Ryu, J. H., Choi, J. K., & Lee, Y. K. (2014). Potential of remote sensing in management of tidal flats: A case study of thematic mapping in the Korean tidal flats. *Ocean & Coastal Management*, 102, 458–470.

- Sunder, S., Ramsankaran, R., & Ramakrishnan, B. (2017). Inter-comparison of remote sensing sensing-based shoreline mapping techniques at different coastal stretches of India. *Environmental Monitoring & Assessment*, 189(6), 290.
- Syvitski, J. P. M., Kettner, A. J., Overeem, I., Hutton, E. W. H., Hannon, M. T., Brakenridge, G. R., Day, J., Vörösmarty, C., Saito, Y., Giosan, L., & Nicholls, R. J. (2009). Sinking deltas due to human activities. *Nature Geoscience*, 2(10), 681–686.
- Vermote, E. F., El Saleous, N., Justice, C. O., Kaufman, Y. J., Privette, J. L., Remer, L., Roger, J. C., & Tanré, D. (1997). Atmospheric correction of visible to middle-infrared EOS-MODIS data over land surfaces: Background, operational algorithm and validation. *Journal of Geophysical Research Atmospheres*, 102(D14), 17131–17141.
- Wang, H. J., Yang, Z. S., Li, G. X., & Jiang, W. S. (2006). Wave climate modeling on the abandoned Huanghe (Yellow River) delta lobe and related deltaic erosion. *Journal of Coastal Research*, 22(4), 906–918.
- Wang, H. J., Bi, N. S., Saito, Y., Wang, Y., Sun, X., Zhang, J., & Yang, Z. (2010). Recent changes in sediment delivery by the Huanghe (Yellow River) to the sea: Causes and environmental implications in its estuary. *Journal of Hydrology*, 391(3–4), 302–313.
- Wang, M., Qi, S., & Zhang, X. (2012). Wetland loss and degradation in the Yellow River delta, Shandong Province of China. *Environmental Earth Sciences*, 67(1), 185–188.
- Wang, Z. B., Maren, D. S. V., Ding, P. X., Yang, S. L., Prooijen, B. C. V., Vet, P. L. M. D., et al. (2015). Human impacts on morphodynamic thresholds in estuarine systems. *Continental Shelf Research*, 111, 174–183.
- Wells, J. T. Jr., A, C. E., Park, Y. A., & Frankenberg, E. W. (1990). Morphology, sedimentology and tidal channel processes on a high-tide-range mudflat, west coast of South Korea. *Marine Geology*, 95(2), 111–130.
- Werf, J. V. D., Reinders, J., Rooijen, A. V., Holzhauer, H., & Ysebaert, T. (2015). Evaluation of a tidal flat sediment nourishment as estuarine management measure. *Ocean & Coastal Management*, 114, 77–87.
- Xu, J. (2000). Land cover and vegetation change in the Yellow River delta nature reserve analyzed with Landsat Thematic Mapper data. *Geocarto International*, 15(4), 43–50.
- Xu, Z., Kim, D. J., Kim, S. H., Cho, Y. K., & Lee, S. G. (2016). Estimation of seasonal topographic variation in tidal flats using waterline method: A case study in Gomso and Hampyeong Bay, South Korea. *Estuarine Coastal & Shelf Science*, 183, 213–220.
- Yang, S. L., Ding, P. X., & Chen, S. L. (2001). Changes in progradation rate of the tidal flats at the mouth of the Changjiang (Yangtze) river. *China Geomorphology*, 38(1–2), 167–180.
- Yao, R. J., Yang, J. S., & Yang, J. S. (2010). Quantitative evaluation of soil salinity and its spatial distribution using electromagnetic induction method. *Agricultural Water Management*, 97(12), 1961–1970.
- Zhang, Y. (2011). Coastal environmental monitoring using remotely sensed data and GIS techniques in the modern Yellow River delta, China. *Environmental Monitoring & Assessment*, 179(1–4), 15–29.
- Zhang, K., Douglas, B. C., & Leatherman, S. P. (2004). Global warming and coastal erosion. *Climatic Change*, 64(1–2), 41–58.
- Zhang, T. T., Zeng, S. L., Gao, Y., Ouyang, Z. T., Li, B., Fang, C. M., & Zhao, B. (2011). Assessing impact of land uses on land salinization in the Yellow River delta, China using an integrated and spatial statistical model. *Land Use Policy*, 28(4), 857–866.
- Zhang, X., Zhang, Y., Ji, Y., Zhang, Y., & Yang, Z. (2016). Shoreline change of the northern Yellow River (Huanghe) delta after the latest deltaic course shift in 1976 and its influence factors. *Journal of Coastal Research*, 74(74), 48–58.